GNSS Radio Occultation Soundings from Commercial Off-the-Shelf Receivers Onboard Balloon Platforms

Kevin J. Nelson[1,*], Feiqin Xie[1], Bryan C. Chan[2], Ashish Goel[2], Jonathan Kosh[2], Tyler G. R. Reid[2], Corey R. Snyder[2], Paul M. Tarantino[2]

[1] Texas A&M University – Corpus Christi, Corpus Christi, TX

[2] Night Crew Labs, LLC, Woodside, CA

[*] Author now at Jet Propulsion Laboratory, California Institute of Technology, Pasadena, CA: kevin.j.nelson@jpl.nasa.gov

Abstract

The global Navigation Satellite System (GNSS) radio occultation (RO) technique has proven to be an effective tool for Earth atmosphere profiling. Traditional spaceborne RO satellite constellations are expensive with relatively low sampling density for specific regions of interest. In contrast, airborne RO platforms can provide much higher spatial and temporal sampling of ROs around regional weather events. This study explores the capability of a low-cost and scalable Commercial-Off-The-Shelf (COTS) GNSS receiver onboard high-altitude balloons. The refractivity retrievals from balloon-borne RO payloads obtained from two flight campaigns (World View and ZPM-1) are presented. The balloon-borne RO soundings from the World View campaign show high-quality refractivity profiles between 6 and 19 km with near-zero median difference from the colocated ECMWF ERA5 reanalysis data and variability comparable to spaceborne RO missions (~2.3% median-absolute-deviation). Soundings from the ZPM-1 campaign show a relatively large positive bias (~2.5%). In summary, low-cost COTS RO payloads onboard balloon platforms are worth further engineering and study in order to provide capabilities for dense, targeted atmospheric soundings that can improve regional weather forecasts via data assimilation.

Deleted: *rates for individual satellites*

Deleted: *A*

Deleted: *paper*

Deleted: *in the troposphere*

Deleted: *from the colocated ECMWF ERA5 reanalysis data*

Deleted: *the*

Deleted: *improvement for*

Deleted: *to*

1. Introduction

The radio occultation (RO) atmospheric profiling method was first developed to measure planetary atmospheres in our solar system. The first major use of RO was part of the mission to examine atmospheric profiles of Venus as part of the Mariner V mission launched in 1967 (Fjeldbo and Eshleman, 1969; Fjeldbo et al., 1971). Due to vertical atmospheric density gradients, radio signals transmitted from the spacecraft will bend and be slightly delayed when passing through the limb of the planetary atmosphere before arriving at a receiving antenna on Earth. This bending accumulation along the ray path can be precisely measured using excess phase delay, and can be used to derive atmospheric pressure, temperature, and concentration of atmospheric constituents (e.g., sulfuric acid concentrations on Venus). The same method was later applied to Mars (Mariner IX, Kliore et al., 1972; Lindal et al., 1979) and Neptune (Voyager II, Lindal, 1992). Even as recently as 2017, additional RO missions to Venus were underway (AKATSUKI, Imamura et al., 2017).

It was not until the mid-1990s that scientists began to apply RO techniques to the Earth's atmosphere using Global Navigation Satellite System (GNSS) signals as transmitting sources (Kursinski et al., 1996, 1997; Ware et al., 1996). To date, most Earth GNSS RO observations are taken from low-Earth orbiting (LEO) satellite constellations such as the Constellation Observing System for Meteorology, Ionosphere, and Climate (COSMIC-1, Anthes et al., 2008), the GNSS Receiver for Atmospheric Sounding (GRAS, Luntama et al., 2008) onboard the MetOp satellite series, and COSMIC-2 (Schreiner et al., 2020). More recently, several private companies (e.g., Spire, GeoOptics, PlanetiQ) launched CubeSat constellations that can offer RO soundings with comparable quality to the more sophisticated satellite RO missions (Bowler, 2020). The impact of spaceborne RO profile assimilation on global weather forecasts has been ranked second

Deleted: change

Deleted: R

Deleted: the

Deleted: er

Deleted: carbon dioxide

Deleted: late

Deleted:

Deleted: PIRE

Deleted: I

Deleted: such as both COSMIC missions among satellite measurements (Cardinali and Healy, 2014), with its impact varying depending on assimilation methods (Boullot et al., 2014; Harnisch et al., 2013; Ruston and Healy, 2020).

RO observations are also possible from receivers inside the atmosphere, as opposed to the LEO receivers in space. One of the more common in-atmosphere RO platforms is an airplane or drone. Airborne radio occultation (ARO) typically uses custom-built receiver payloads onboard a modified aircraft with additional antennae and is capable of significantly higher spatial sampling density than spaceborne RO (Wang et al., 2016) due to their slower velocities compared to the LEO receiver satellites (e.g., COSMIC-1, COSMIC-2). This allows ARO receivers to potentially track more GNSS signals, creating the potential for more frequent, localized occultations (Chan et al., 2022, 2021; Xie et al., 2008). ARO platforms also have the benefit of providing on-demand RO profiles around transient weather events such as mid-latitude or tropical cyclones. ARO is limited primarily by flight restrictions regulated by the U.S. Federal Aviation Administration, by fuel range of the aircrafts, and by increased tangent point drifting, potentially leading to variations in the sampled atmosphere over the distance of the ray path.

Early ARO studies developed and tested research instruments as a baseline for in-atmosphere RO, as well as modified the traditional spaceborne retrieval algorithms (Garrison et al., 2007; Healy et al., 2002; Xie et al., 2008; Zuffada et al., 1999). Open-loop signal tracking was successfully implemented recently to reduce unwrapping and tracking errors from airborne platforms (Murphy et al., 2015; Wang et al., 2016). Radio-holographic retrieval methods have also been modified for in-atmosphere radio occultations (Adhikari et al., 2016; Wang et al., 2016) have also been implemented to improve upon geometric optics retrievals (Kursinski et al., 1997, 2000) in the moist lower troposphere that suffer from multi-path errors.

Deleted: , such as the full-spectrum-inversion

Deleted: were

Deleted: due to

Another option for an RO observation platform is a high-altitude balloon, but few attempts have been successfully implemented thus far. The Concordiasi Project (Rabier et al., 2013, 2010) is the only field campaign to date during which balloon-borne RO (BRO) observations were targeted as part of the overall research goal. Haase et al., (2012) detailed the proof-of-concept BRO payload and platform design, along with some preliminary results indicating the feasibility of BRO measurements. Other remote sensing projects have used balloon platforms for other purposes (e.g., GNSS Reflectometry (GNSS-R), Carreno-Luengo et al., 2016) but GNSS RO payloads on balloon platforms are still otherwise underrepresented.

Balloon-borne RO has many advantages over spaceborne RO and ARO. Like ARO observations, BRO platforms move slowly compared to spaceborne platforms, and are therefore capable of offering high spatial and temporal sounding densities. Additionally, BRO platforms can remain aloft and collect observations for weeks to months, depending on the design and capabilities of the platforms (Chan et al., 2022, 2021). BRO platforms can also be tactically launched *en masse* above and around transient weather events such as tropical cyclones and supercell thunderstorms to provide spatially dense sampling of atmospheric thermodynamic profiles inside and surrounding dangerous weather events.

Multiple agencies of the U.S. federal government are also invested in obtaining supplementary RO data for the purposes of supporting operational needs. The U.S. National Oceanic and Atmospheric Administration (NOAA) is undergoing a multi-year program intended to incentivize commercial participation in data-as-a-service that can be used for improving weather forecasting through data assimilation (National Oceanic and Atmospheric Administration and National Environmental Satellite, Data, and Information Service, 2020). Furthermore, low-cost, on-demand RO data would be highly useful for conducting research,

Deleted: [*Rabier et al.*, 2010; *Rabier et al.*, 2013]

Deleted:

primarily in the planetary boundary layer (PBL). A targeted observable in the NASA 2017 decadal survey is the PBL (National Academies of Sciences, 2018), and BRO data would be a low-cost alternative or supplement to spaceborne and airborne radio occultation data for identifying PBL characteristics.

The remainder of this paper is structured as follows. Section 2 briefly introduces a newly developed, low-cost and scalable COTS GNSS receiver onboard high-altitude balloons and the associated flight campaigns, along with the detailed description on BRO data and methodology. Section 3 shows the refractivity retrieval process and quality control procedures based on one representative BRO case. Section 4 examines the overall statistics of the BRO observations and provides a preliminary error analysis. Finally, conclusions and future studies are summarized in Section 5.

Deleted: commercial-off-the-shelf (

Deleted:)

2. Data and Methodology

a. Balloon-borne GNSS RO Payload and High-altitude Balloon Platforms

Deleted: the

A detailed description of the balloon-borne GNSS RO payload developed by Night Crew Labs (NCL) can be found in (Chan et al., 2022, 2021) – a summary is presented here. The instrumentation is comprised of two major components: a mission system support component, and a science payload for GNSS RO profiling. The Balloon Re-Programmable Integrated Computer (BRIC) is a third-generation flight management computer supporting data logging as well as power management, flight control, and thermal control. The GNSS Radio Occultation and Observable Truth (GROOT) is a first-generation balloon-borne GNSS RO science instrument based on COTS GNSS equipment. The GROOT payload includes a Swift Navigation Piksi Multi GNSS receiver for raw RO measurements (e.g., carrier phase, SNR, and Doppler velocities), a Trimble BX992 dual-antenna GNSS receiver coupled with an inertial navigation

Deleted: commercial off-the-shelf (

Deleted:)

system and an L-band GNSS corrections service, in addition to the BRIC flight computer and other ancillary needs. All balloon-borne RO data described in this study were collected from the GROOT payload. The Piksi GNSS RO receiver is particularly noteworthy, as it is about the size of a credit card, which is quite small compared to most other custom-built GNSS RO receivers for airborne and spaceborne observations.

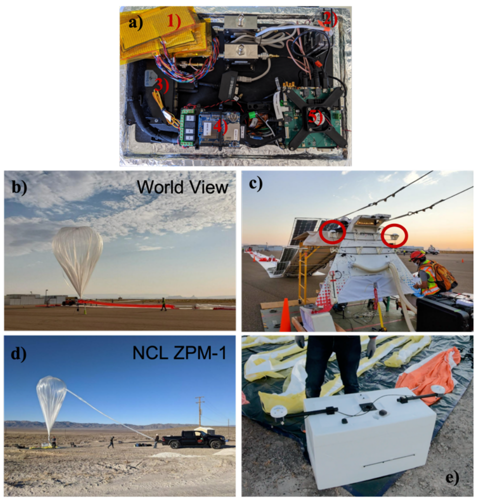

Figure 1: a) GROOT payload used in balloon RO flight missions. Numbers indicate the following components – 1) Patch heaters, 2) Raspberry Pi data logger, 3) Trimble BX992 receiver, 4) BRIC flight computer, 5) Power board/Swift Piksi Multi stack for phase and amplitude measurements (adapted from Chan et al., (2022)); b) World View Stratolite balloon being filled prior to launch. c) Balloon RO payload being prepared for launch during World View BRO flight campaigns. GNSS antennae are indicated by red circles. d) NCL ZPM balloon being filled prior to launch. e) ZPM-1 RO payload and GNSS antennae configuration.

In this study, the RO profiles collected from two high-altitude balloon flight campaigns equipped with the GROOT payload were analyzed. Figure 1a shows the GROOT payload as described above, with each component labeled. The first of a series of high-altitude balloon campaigns occurred in August 2020 on a zero-pressure balloon as a secondary payload hosted on the World View Stratolite balloon bus platform (Fig. 1b, c). The World View flight launched out of Page, AZ and maintained 18+ km (60,000+ ft) altitude, enabling five days (120 hours) of continuous data collection. During the flight, GROOT continuously collected balloon state data and RO data from the GPS (United States), GLONASS (Russia), Galileo (European Union), BeiDou (China), and QZSS (Japan) constellations. The World View balloon platform was equipped with yaw control equipment to keep it from spinning during flight. After mission termination, the data was recovered and processed.

The second flight campaign was the NCL Zero Pressure Balloon Mission 1 (ZPM-1), which launched near Empire, NV on November 28, 2020 (Fig. 1d, e). The ZPM-1 balloon reached a maximum altitude of 31.7 km (104,567 ft), traveling southeast towards Utah. Overnight, ZPM-1 dropped to a lower-than-expected altitude of 17.9 km (59,000 ft) due to colder ambient temperature, which caused the balloon to drift eastwards towards the Rocky Mountains and led to termination of the mission after 12 hours. During the flight, GROOT collected balloon state data and RO data from GPS, GLONASS, Galileo, BeiDou and QZSS constellations. The payload was later recovered in southern Utah.

Deleted: was

b. Balloon-Borne RO Measurements

Figure 2 shows the ground tracks for the two balloon flight campaigns along with the predicted occultation tangent point locations at the lowest elevation angle, labeled by their respective GNSS RO satellites. The selected occultation events extracted for analysis are highlighted for both flight campaigns.

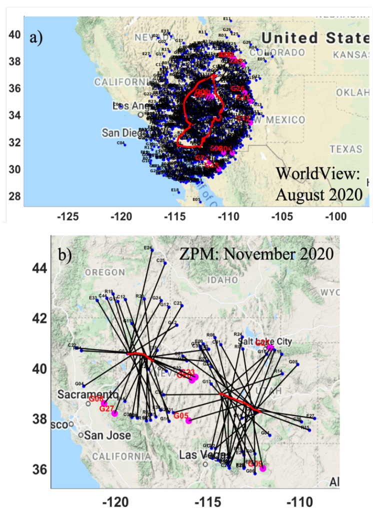

Figure 2: High-altitude balloon flight trajectory (red) and predicted occultation tangent point drifting paths and their respective GPS satellites (black) for a) World View and b) ZPM. Pink circles with red text indicate the selected RO cases and the occulting GPS satellite number presented in this study.

The GROOT receiver can potentially track all currently operational GNSS satellite constellations such as GPS, GLONASS, Galileo, BeiDou, and QZSS. However, only the GPS signals were chosen to be tracked due to the limited bandwidth capability of the receiver. Out of a total number of 680 predicted occultation soundings for the World View flight (based on balloon and GNSS real trajectories), approximately 71% of observations came from non-GPS occultations and were not analyzed (see Fig. A1). This decision was made because GROOT processing on non-GPS satellites data from several previous flights consistently resulted in poor quality ROs as a result of receiver frequency capabilities. In addition, the closed-loop tracking receiver in the GROOT payload can only track setting (vs. rising) occultations, filtering out another 50% of the available occultations. Of the remaining occultations, only the RO events having measurements with 1) minimum elevation angle less than 0°, and 2) excess phase greater than 50 meters were processed. This subset of occultations were divided into those that are good quality and those

Deleted: due to the limited bandwidth and capability of the receiver, …

Deleted: with high enough quality

Deleted: o

that require additional quality control such as cycle-slip corrections (Fig. A1). Of the original 680 occultations from the World View flight, only 15 cases were extracted for analysis (see Appendix A). Cycle slip corrections were required for 7 of the 15 cases, and one World View case was removed after failing quality control procedures. The same pre- and post-processing algorithms were applied to ZPM-1 measurements. Unfortunately, the ZPM-1 flight encountered power failures during the segments of the flight, resulting in the loss of altitude and a much shorter flight time with fewer occultations being collected, and only 8 occultations out of 84 were selected for processing.

c. Balloon-Borne RO Data Processing and Retrieval Methods

After the flight data is logged, several processing steps are required to retrieve bending angle and refractivity. The full retrieval process is detailed in (Chan et al., 2022), but is summarized here. The first step in the BRO retrieval is to pre-process the data for ingestion into the retrieval algorithms. Raw line-of-sight (LOS) GNSS observables, along with satellite ephemeris data, and balloon state (position/velocity) data are extracted from payload storage. Once the LOS data is parsed and aligned, the next step is to compute the excess phase delay (or excess phase) by subtracting the receiver's measured phase from the LOS geometric distance between the GNSS satellite and the receiver, based ephemeris data from a high-elevation satellite. Step three is receiver clock calibration, where the excess phase is calibrated by differencing the excess phase of the occulting and high-elevation GNSS satellites. Step four is cycle slip correction, where an exponential curve is fitted to the data to both smooth and remove medium to large discontinuities. Step five uses a Gaussian Process Regression (GPR, Shi and Choi, 2011) to further remove any smaller discontinuities as needed in processing the individual cases. Steps three through five clean and smooth the excess phase data so that it can be used in

Deleted: 3

Deleted: good

Deleted: Similar

Deleted: processes

Deleted: on

Deleted: ephemeris data

Deleted: 5

the retrieval downstream in the retrieval processing. Finally, the processed result: RO excess phase delay, excess Doppler shift, SNR, and balloon state are exported as a NetCDF file, a format convenient for downstream GNSS RO retrieval processing.

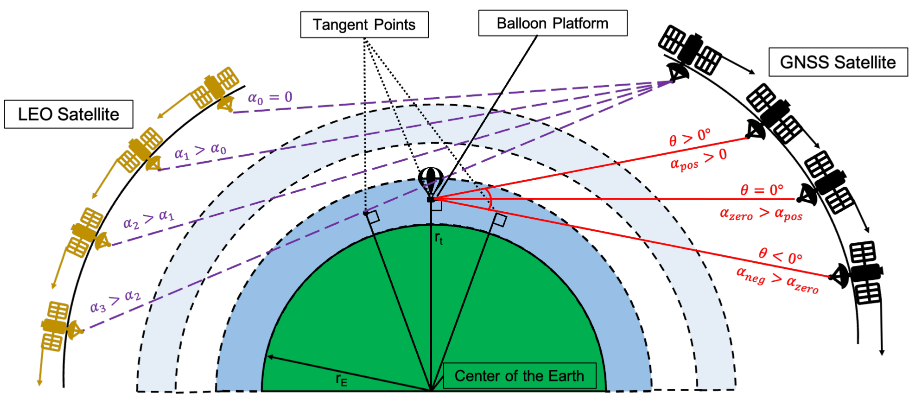

Figure 3: Balloon radio occultation transmitter/receiver geometry diagram. Adapted from (Xie et al., 2008). r_E and r_t represent the radius of the earth and the radius at the tangent point, respectively.

Traditional spaceborne RO for Earth's atmosphere has a very well-known transmitter/receiver geometry. Because balloon-borne (and airborne) radio occultations have a more unique, less common geometry we discuss it here. Figure 3 shows the geometry for a balloon-borne radio occultation, in conjunction with a more traditional spaceborne RO geometry. The receiver onboard the balloon platform is shown in the center at a radius r_t. High-elevation GNSS satellites, where the elevation angle is required to be $\theta > 55°$, are used to calibrate the excess phase delay at the in-atmosphere receiver. GNSS satellites with elevation angle $-5° < \theta < 5°$ are used in the retrieval process to calculate the bending angle retrievals and subsequent products (Chan et al., 2022; Xie et al., 2018).

To evaluate the performance of the balloon-borne GNSS-RO retrieval algorithm, an end-to-end simulation and retrieval processing system (Figure 4) originally developed for aircraft-based GNSS RO (Xie et al., 2008) was adapted for balloon-borne RO measurements. The

Deleted: The
Deleted: h
Formatted: Font: Italic
Formatted: Font: Italic, Subscript
Deleted: is shown
Formatted: Font: Italic
Deleted: The
Deleted: 3
Deleted: [*Xie et al.*, 2008]
Deleted: the

processing system includes four main components: (a) a geometric optics ray-tracer (i.e., Radio Occultation Simulations for Atmospheric Profiling (ROSAP, Høeg et al., 1996)), which simulates the GNSS RO signal excess phase delay/Doppler as it travels through a Earth's atmosphere defined as either spherically symmetric or oblately symmetric prescribed by a given atmospheric refractivity profile and accumulates bending at each iteration. The oblate atmosphere option is used in our study.; (b) a module that derives the bending angle from the LOS excess phase/Doppler measurements through a modified geometric-optics (GO) retrieval (i.e., Doppler-to-alpha, (Lesne et al., 2002; Vorob'ev and Krasil'nikova, 1994; Xie et al., 2008)) and radio-holographic retrieval (i.e., full-spectrum-inversion, FSI) modified for in-atmosphere retrievals (Adhikari et al., 2016; Jensen et al., 2003); (c) a forward Abel integrator (FAI) modified for in-atmosphere retrievals that generates the bending angle profile through the forward integration of an input refractivity profile (Fjeldbo and Eshleman, 1969; Fjeldbo et al., 1971; Xie et al., 2008); and (d) an inverse integrator that retrieves a refractivity profile via an Inverse Abel Transform (IAT, Fjeldbo and Eshleman, 1969) modified for in-atmosphere RO (Healy et al., 2002; Xie et al., 2008).

Deleted: spherically symmetric

Deleted: [*Adhikari et al.*, 2016; *Jensen et al.*, 2003]

Deleted: airborne

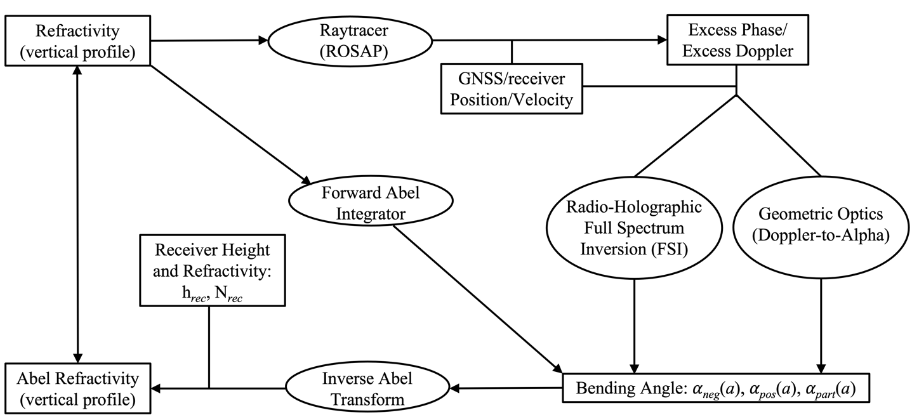

Figure 4: Flow chart of the end-to-end simulation and retrieval processing system for airborne and balloon-borne GNSS radio occultation.

Deleted: 3

Note that the GO retrieval method has limited vertical resolution and encounters multipath problems in the moist lower troposphere. Therefore, the FSI method adapted for airborne and balloon-borne RO retrieval will also be used (Adhikari et al., 2016).

After the bending angle (α) profiles are retrieved using either GO or FSI methods, the partial bending angle (α_{part}), i.e., the difference between negative and positive elevation bending angles (α_{neg} and α_{pos}) at same impact parameter, can be derived. The partial bending angle profile is then converted to the refractivity profile using the modified IAT, which requires *a priori* knowledge of the refractivity at the receiver during the occultation event. In addition, the local radius of curvature of the earth is also required for conversion of bending angle impact parameter to geometric height as part of the IAT. Due to the very low excess phase delay, the raw observation of α_{pos} as well as the α_{neg} near the receiver height is generally very small and can also be rather noisy or reach a singularity, which would lead to large errors in partial bending angle and the following refractivity retrieval. Therefore, in this study, the α_{pos} and the α_{neg} within 1.5 km of the receiver were substituted by the simulated bending angle (e.g., FAI or ROSAP bending angle simulation) based on a colocated refractivity profile (Adhikari et al., 2016; Xie et al., 2018). By doing this, the top 1.5 km of the α_{pos} and the α_{neg} profiles are significantly less noisy and chaotic, preventing failure of the IAT.

d. ERA5 Model Reanalysis Data

To evaluate the quality of balloon-borne RO measurements, we use 3-hourly ERA5 model reanalysis (Hersbach et al., 2020) from the European Centre for Medium-range Weather Forecasting (ECMWF) to provide estimates of atmospheric conditions near the BRO sounding locations. The native ERA5 model grid has 0.25°x0.25° horizontal resolution and 137 vertical levels. The ERA5 profiles are referenced to geopotential heights, which are converted to

Deleted: c

Deleted: so

Deleted: full

Deleted: ~

Deleted: below

Deleted: the

Deleted: reanalysis

geometric heights for direct comparisons to BRO profiles. The atmospheric refractivity profiles can be derived from the gridded temperature, humidity, and pressure profiles.

In addition, during an occultation event, the tangent point is located at the receiver position, when the occulting satellite is at the zero elevation. In-atmosphere RO bending angle retrieval requires *a priori* atmospheric refractivity at the receiver, which can be provided by the colocated ERA5 profile, when high-quality in-situ measurements are not available (Xie et al., 2018, 2008; Adhikari et al., 2016). Thus, for simplicity, each occultation event uses one refractivity profile from the colocated ERA5 grid (at the zero-elevation ($\theta = 0$) angle tangent point location) to compute the time series of refractivity at the receiver by interpolating the refractivity profile to the receiver height at each time stamp throughout the occultation observations. Furthermore, considering the high horizontal resolution of ERA5 reanalysis and the potential fine scale variations of refractivity that are smaller than RO horizontal footprint, we use a median refractivity profile of a 1°x1° horizontal grid surrounding the zero-elevation location for input into the initial ROSAP and FAI simulations. The tangent point locations during the occultation event can therefore be derived from ROSAP ray-tracing simulation with the real occultation geometry. It is important to consider the potentially large horizontal drift associated with the tangent point of BRO observations. To better evaluate the quality of the individual retrieved BRO refractivity profiles, the ERA5 profile tangent point location at 5 km altitude will be treated as the BRO colocated profile for the final refractivity comparison.

Deleted: The airborne

Deleted: zero elevation

Deleted: resolution

Deleted: space

Deleted:

Deleted: considering the large tangent point drifting distance

Deleted: above mean-sea-level (MSL)

Deleted: purposes

3. Case Study: BRO from the World View Campaign

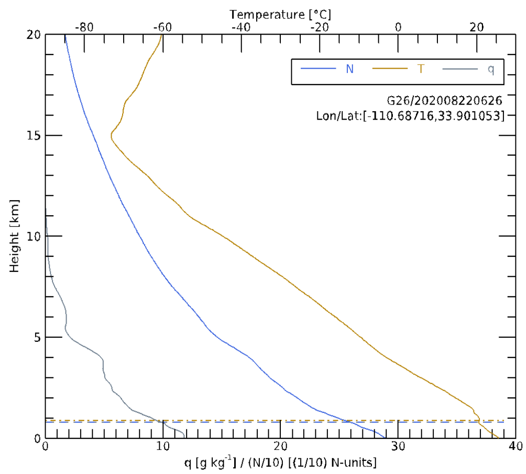

Figure 5: ERA5 vertical profiles of temperature (gold), specific humidity (q, grey), and refractivity (N, blue) at 0600 UTC colocated with the World View G26 BRO case on August 22, 2020. Note that for display purpose, one-tenth of the refractivity (N/10) was plotted. In addition, the colocation longitude and latitude of the BRO profile are indicated.

Here we focus on one typical BRO sounding, an approximately 27-minute-long BRO measurement from the World View campaign (hereafter referred to as WVG26) at 06:26 UTC, August 22, 2020. The WVG26 case occurred over the Tonto National Forest, northeast of Phoenix, Arizona. The colocated ERA5 thermodynamic profiles (temperature, specific humidity, and refractivity) at the location of this BRO sounding with tangent point at 5 km above mean-sea-level are shown in Figure 5. During the occultation event, the local atmosphere was hot and very dry, particularly above 5 km. Additionally, planetary boundary layer height (PBLH) for this case was found to be at approximately 0.9 km, clearly marked by a distinct temperature inversion and weak gradients in specific humidity, and refractivity (dashed lines, Fig. 5). The cold-point tropopause was located around 15 km altitude.

Deleted: *4*

Deleted: 4

Deleted: the top of the boundary layer

Deleted: 4

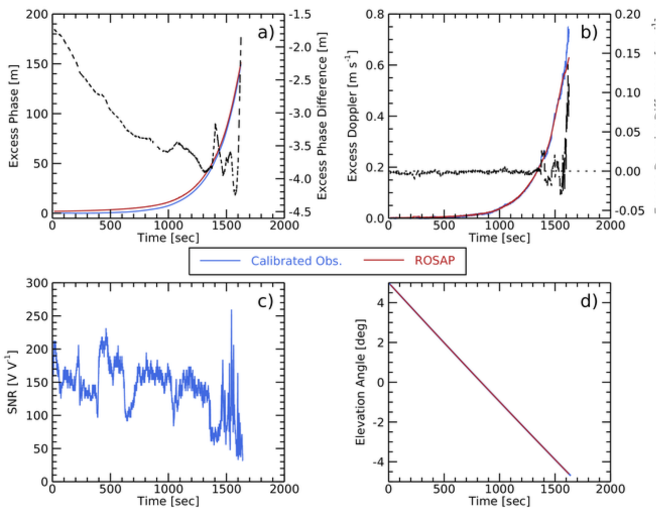

Figure 6: WVG26 time series of a) excess phase, b) excess Doppler, c) signal-to-noise ratio, and d) elevation angle from calibrated observations (blue), and ROSAP ray-tracing simulation (red). Dashed lines in panels a) and b) represent

Figure 6a shows the WVG26 calibrated excess phase delay observations (blue) alongside the excess phase delay from the ROSAP simulation (red) and their differences (black dashed line). The calibrated excess phase delay compares favorably with the colocated ROSAP excess phase delay, with differences between the two within three meters of each other throught the whole time series. The high consistency throughout the time series is also seen in the excess Doppler comparison (Fig. 5b) with differences only exceeding 0.01 m s^{-1} at the end of the time series. The observed signal-to-noise ratio (SNR) for the WVG26 case is shown in Figure 6c. As the signal penetrates deeper into the atmosphere (i.e., the elevation angle dipping below the local horizon to approximately – 4.5°, Fig. 6d), the SNR typically decreases and becomes much more variable due to high signal dynamics resulting from the fine moisture variations in the lower troposphere. The overall mean SNR from the GROOT receiver (141.79 V V^{-1}) is on the same order of magnitude (order of 100) as the mean SNR from the COSMIC-1 and SAC-C GNSS RO

Deleted: *5*
Deleted: *raw observations (black),*
Deleted: *red*
Deleted: *green*
Deleted: 5
Deleted: raw and
Deleted: ERA5
Deleted: -derived
Deleted: (obtained using ROSAP raytracing simulation)
Deleted: but shows larger variation in the ROSAP results, likely due to satellite-receiver geometry fluctuations.
Deleted: 5
Deleted: 5

satellite missions (approximately 700 V V^{-1}, Ao et al., 2009; Ho et al., 2020). While the SNR values from the Piksi receiver are still approximately 5 times less than the values from spaceborne RO missions, the compact size of the Piksi receiver makes such high SNR values quite impressive.

Figure 7a shows the BRO bending angle profiles from GO and FSI retrievals as a function of impact height (impact parameter minus the local curvature radius of the Earth) for the WVG26 case. Note that as discussed in Section 2c, the noisy α_{pos} and α_{neg} within 1.5 km below the receiver height were replaced by the simulated FAI bending angle based on the colocated ERA5 refractivity profile (Fig. 5). Fig. 7a also shows a conceptual calculation of the partial bending angle as discussed in Section 2c. At each impact height, α_{pos} is subtracted from α_{neg} to calculate the partial bending angle (α_{part}), which is later used to retrieve the final refractivity profile. Figure 7b shows the partial bending angle calculated using the method shown in Fig. 7a with 100 m log-linear vertical smoothing applied. It is worth noting that BRO bending angle observations from both the GO and FSI retrievals match the colocated ERA5 FAI and ROSAP simulations quite well from the balloon altitude (just over 18 km) all the way down to impact heights of around 6 km (corresponding to approximately 4 km above MSL, Fig. 7). Differences between the retrievals and the ROSAP simulation between ~ 6 and 8 km are most likely caused by differences between oblate and spherical Earth geometry assumptions. While an Earth oblateness correction is performed as part of the transmitter/receiver geometry processing, these effects may not be completely removed.

Deleted: [700 V V^{-1}, *Ao et al.*, 2009; *Ho et al.*, 2020]

Deleted: Considering the size of the Piksi receiver on the GROOT payload, this is quite impressive.

Deleted: Given the excess phase/Doppler measurements, the accumulated bending angle from GO and FSI retrievals as a function of impact height (impact parameter minus the local curvature radius of the Earth) for the WVG26 case are shown in Fig. 6a.

Deleted: 4

Deleted: 6

Deleted: b

Deleted: 6

Deleted: 6

Deleted: 6

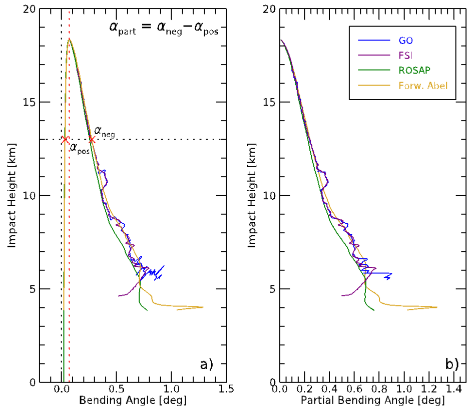

Figure 7: a) Bending angle for WVG26 case from the GO retrieval (blue) and FSI retrieval (purple), in comparison with the colocated ERA5 bending angle from ROSAP ray-tracing simulation (green), and forward-Abel-integrator (gold). Conceptual calculation of partial bending angle at 13 km impact height is also shown. b) Final partial bending angle for WVG26 case from the GO retrieval (blue), FSI retrieval (purple), ROSAP ray-tracing simulation (green), and Forward Abel transform (gold).

Deleted: *6*

Figure 8a shows the refractivity retrieval for the WVG26 BRO case. The 5 km tangent height ERA5 refractivity profiles colocated with the WVG26 case is approximately 425 km from the receiver location, and the terrain changes significantly compared to the origin point in the Tonto National Forest. From the top of the refractivity profiles, both the GO and FSI retrievals match the ERA5 refractivity profile from the location of the 5 km tangent height very well. Similar to the α_{part} results, the refractivity retrieval from FSI bending angle reaches about 1 km deeper into the atmosphere than the GO retrieval, highlighting the usefulness of the FSI over GO

Deleted: 7

methods. This is primarily due to the improvement from FSI on resolving the multipath problem over the GO method in the moist lower troposphere.

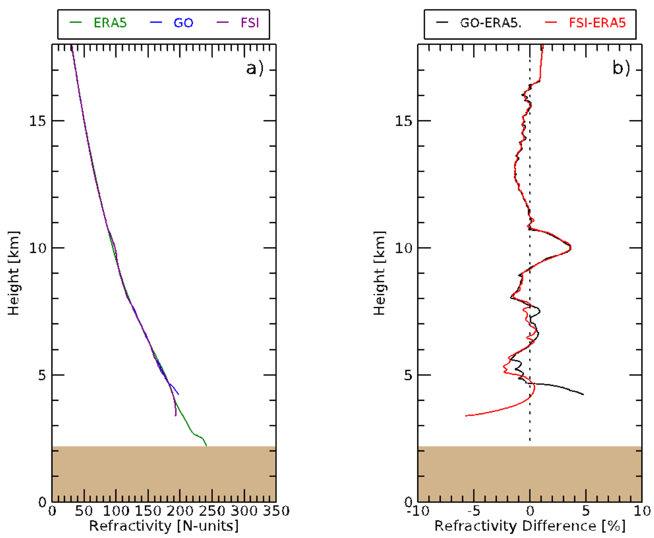

Figure 8: a) BRO refractivity retrieval for WVG26 case from GO (blue) and FSI (purple) compared to the colocated refractivity profile from ERA5. b) Fractional refractivity difference between BRO retrieval and ERA5 (GO, black; FSI, red). Local terrain at the location of BRO tangent point at 5 km above MSL is marked by tan polygons.

In order to quantify the differences between the retrievals and the colocated ERA5 profile, the fractional refractivity difference profile is calculated. Figure 8b shows the fractional refractivity difference between the refractivity retrievals (GO and FSI) and their colocated ERA5 profiles, respectively. The GO retrieval is highly consistent with FSI retrieval above ~7.5 km and start showing small differences below. Above 10 km, the median refractivity difference profiles for the GO-ERA5 and FSI-ERA5 are -0.27% to -0.26% with a median-absolute-deviation (MAD) of approximately 0.62%. Both retrievals continue to perform very well in the middle troposphere, between 5 km and 10 km with median refractivity differences of -0.21±0.74% for the GO retrieval and -0.38±0.59% for the FSI retrieval. Once more water vapor is encountered below 5 km altitude, the magnitude of the median difference for the GO retrieval increases to

Deleted: *7*

Deleted: 7

Deleted: GO/FSI

Deleted: s

Deleted: s

Deleted: between the retrievals and the colocated 5 km tangent height ERA5 profile

Deleted: both

Deleted: /MAD

1.67±2.12%. The refractivity difference for the FSI retrieval remains comparable to the higher altitude overall refractivity difference estimates at -0.24±0.57%. Additionally, signal loss due to platform yaw rotation induces retrieval errors in the FSI retrieval and stops the GO retrieval, resulting in the sharp decrease/increase in *N*-bias for FSI and GO, respectively.

Formatted: Font: Italic

4. Evaluation of Balloon-Borne RO Refractivity Retrievals

Figure 9 shows the fractional refractivity difference between GO/FSI retrievals and the colocated ERA5 profile for each BRO sounding from the World View flight campaign. Individual fractional refractivity difference profiles are calculated by interpolating the retrieval and ERA5 profiles to the same 10 m vertical grid before taking difference between the refractivity profiles. Summary statistics for the World View flight campaign calculated over different height ranges are shown in Table 1. The median refractivity difference between the GO retrieval and the colocated ERA5 oscillates within 0.25% with MAD between 0.71% above 15 km and approximately 2.28% across all levels (see Table 1). The GO refractivity retrieval starts

Deleted: 8

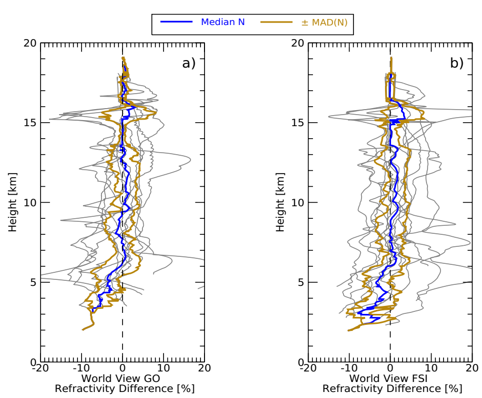

Figure 9: Fractional refractivity difference between BRO retrievals and the colocated ERA5 for: a) GO retrievals and b) FSI retrievals of all World View cases (grey). The median fractional refractivity difference profiles are shown in blue and the median +/- the median absolute deviation (MAD) is shown in gold.

Deleted: *8*

showing negative *N*-bias below approximately 6 km, with a median refractivity difference of -5.86% (MAD: 1.99%) over the 0-5 km height range. The FSI retrieval also starts showing

Deleted: The GO refractivity retrieval starts

Deleted: with the minimum bias

negative *N*-bias below approximately 6 km, but with a smaller median difference of -3.60% (MAD: 3.26%). The higher magnitude *N*-bias in the lowest portions of the troposphere have a variety of potential causes. The lowest level negative *N*-bias is likely caused by the tracking errors (e.g., cycle slips) introduced by the closed-loop tracking receiver, which is a well-known problem (Ao et al., 2009; Wang et al., 2013) that could easily degrade the BRO observation quality. Additionally, high spatial variations in moisture content can also cause low SNR or high signal dynamics ultimately resulting in unwrapping errors in excess phase and hence a negative bending angle bias (Wang et al., 2016). It is also important to consider that there is likely to be increased low-sampling bias closer to the surface, weakening the robustness of the statistics.

Moved (insertion) [1]

Moved up [1]: (Ao et al., 2009; Wang et al., 2013)

Deleted: Furthermore

Table 1: Summary statistics for median refractivity differences between GO/FSI retrievals and the colocated ERA5 with corresponding median absolute deviation over varying height ranges from the World View flight campaign.

Height Range [km]	GO Median *N* Difference [%]	FSI Median *N* Difference [%]
0-5	-5.86 ± 1.99	-3.60 ± 3.26
5-10	-0.25 ±2.97	0.32 ± 3.06
10-15	0.57 ± 2.44	1.06 ± 2.29
15-20	0.53 ± 0.71	0.23 ± 0.94
Overall	0.03 ± 2.28	0.24 ± 2.61

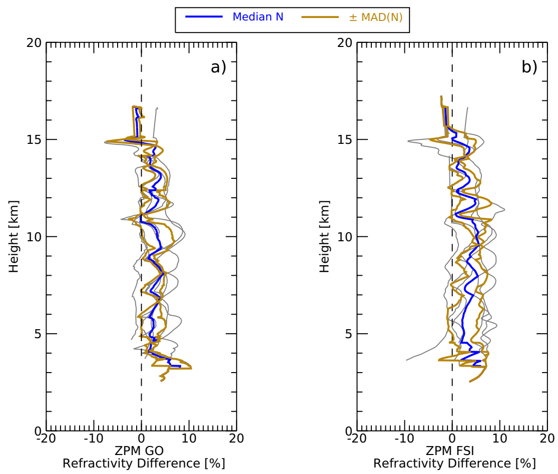

Figure 10: Same as Figure 8, but for the ZPM-1 flight campaign.

Deleted: *8*

Figure 10 shows the fractional refractivity difference profiles for the ZPM-1 flight campaign from the GO and FSI retrievals. The ZPM-1 refractivity differences from both retrieval methods show much more variability in the form of "oscillations" across all heights in both the median profile and the individual refractivity profiles. The ZPM-1 refractivity differences are also slightly positively biased overall compared to the World View campaign data. The GO retrieval has an overall median refractivity difference of 2.57% (MAD: 1.38%). The maximum *N*-bias from the GO retrieval is 4.05% in the lower troposphere. The FSI retrieval has an overall median refractivity difference of 3.13% (MAD: 2.03%). The World View platform had rotational yaw control capability, whereas the ZPM-1 platform did not – as such, the platform and GNSS antennae were free to spin during high-altitude wind gusts. During RO events, rotational movement likely induced position errors in the dual-antenna navigation system, which could result in higher noise and larger *N*-bias. Such a phenomenon warrants future investigation for BRO platforms, as well as how to best control the platform orientation.

Deleted: 9

Deleted: s

Deleted: and is

Deleted:

Deleted: and

Table 2: Same as Table 1, but for the ZPM-1 flight campaign.

Height Range [km]	GO Median *N* Difference [%]	FSI Median *N* Difference [%]
0-5	4.05 ± 0.99	4.01 ± 2.15
5-10	2.94 ± 1.56	3.59 ± 2.29
10-15	2.57 ± 1.78	3.03 ± 1.73
15-20	-0.94 ± 0.64	-1.33 ± 0.47
Overall	2.57 ± 1.38	3.13 ± 2.03

Reasons for errors and bias in BRO refractivity retrievals can come from a variety of potential causes. The limitations of closed-loop tracking receivers may affect the BRO refractivity retrieval quality as discussed above. Additionally, low SNR in airborne (in-atmosphere) GNSS RO observations can potentially result in approximately ±5% refractivity error (Wang et al., 2016). This estimate is consistent with the overall results showed here, meaning that an improvement to SNR in the lower atmosphere would be extremely beneficial. However, it is important to note that despite the overall positive bias in the ZPM-1 cases, the median absolute deviation of the cases minimizes in the upper and middle troposphere, much like the World View campaign data. One important caveat for the ZPM-1 campaign data is the small number of available occultations. Power loss issues on the platform during the flights caused a decrease in the number of occultations. The low sampling numbers could also lead to larger median refractivity differences.

Deleted: also

Deleted: the

Deleted: could

5. Summary and Conclusions

In this study, the GNSS RO atmospheric profiling technique has been adapted for use on high-altitude balloon platforms. Most of the past airborne and balloon-borne RO payloads require custom made parts and costly operational expenses that require significant investments. We show the successful implementation of the Night Crew Labs GROOT payload developed from commercial off-the-shelf components on high-altitude balloon platforms. This approach is simpler and significantly more affordable than current airborne and space-based methods. The results from the low-cost, highly compact GROOT payload are promising.

Deleted: their

Utilizing a balloon platform for GNSS RO observations has been done only once in the past. Haase et al., (2012) showed the proof-of-concept for balloon-borne GNSS RO using a custom-built receiver and found excess Doppler agreement that would correspond to approximately 1% refractivity difference. The BRO retrievals from the GROOT payload have refractivity differences in the middle and upper troposphere comparable to previous airborne and balloon-borne RO studies (Adhikari et al., 2016; Haase et al., 2012; Xie et al., 2008; Healy et al., 2002). The added benefit of using BRO platforms is the dense spatial and temporal sampling available due to the low platform velocities relative to the LEO-based RO satellites. Additionally, BRO platforms are scalable and can potentially be launched in advance of significant weather events and remain aloft for long periods of time to collect abundant RO observations.

Currently, the major limitation of BRO platforms with COTS payloads is the use of closed-loop tracking GNSS receivers. For GNSS RO purposes, closed-loop tracking can limit penetration of retrieved refractivity profiles into the lower troposphere due to the large variations in moisture content. Additionally, closed-loop tracking also prohibits the tracking of rising occultations, cutting the potential number of RO soundings in half. For these reasons, design and implementation of COTS payloads capable of open-loop tracking is the next natural step to improving balloon-borne RO. Furthermore, BRO platform orientation can be uncontrolled, so a sudden change in winds aloft can alter the antenna position and cause signal loss. Additionally, the comparatively slow-moving receivers result in longer occultations (approximately 20-30 minutes for one balloon-borne RO event, in comparison to ~1 minute for one spaceborne RO

Deleted: , which is commercially available event), which can result in larger unwrapping error (Wang et al., 2016) and lead to further underestimates of bending angle in the moist lower troposphere.

An analysis of the quality of the retrieved refractivity profiles reveals that the median refractivity difference for the World View campaign is generally less than 1%. The same analysis of the ZPM-1 campaign data shows that the median is slightly positively biased overall (approximately 3%), but with similar median absolute deviation values. While both GO and FSI retrieval methods offer promising results, it appears that the FSI retrievals tend to outperform the GO retrievals in terms of atmospheric penetration. The limitation of the close-loop tracking could be the primary cause of the negative *N*-bias below 6 km as seen in World View BRO soundings. In addition, the relatively low SNR in the lower troposphere could also lead to negative bending angle bias, which could also be another likely cause of the negative refractivity bias in the lower troposphere.

Overall, we show that high-altitude balloons with RO payloads can be launched over areas of complex terrain, can potentially remain aloft for far longer than airborne RO platforms, and would hypothetically be deployable in all weather conditions, similar to radiosondes. Furthermore, the balloon-borne RO platform can offer unprecedented high spatial and temporal BRO sampling over targeted regions far higher than traditional spaceborne RO (see Fig. 2). Additionally, balloon-borne RO data could be much more cost effective to retrieve due to the low-cost COTS GNSS receiver and overall affordability of the high-altitude balloon flight platform, as the instrument can be retrieved and reused after each deployment. We wish to emphasize that results from this proof-of-concept study are likely not enough to truly determine the full capability and limitation of COTS BRO, and that further investment and development will likely yield a more complete picture. We believe the advances on the COTS GNSS receiver

Deleted: in all weather conditions,

Deleted: and

Deleted: Therefore

development and high-altitude balloon platform control in the future will lead to large increases in high-quality localized BRO soundings over targeting weather events (e.g., severe thunderstorms etc.) and improve regional weather forecasts through data assimilation.

6. Acknowledgements

This paper is supported by NOAA grant 1305M2-19-C-NRMW-0015. Author K. Nelson acknowledges the research assistantship support from Coastal Marine System Science Program at Texas A&M University – Corpus Christi. Authors from Night Crew Labs acknowledge additional support from NASA grant 80NSSC20K0106. This work was done as a private venture and not in the authors' capacity as an employee of the Jet Propulsion Laboratory, California Institute of Technology. The authors would also like to thank Dr. Loknath Adhikari from the University of Maryland for productive discussion. The anonymous reviewers are also acknowledged for their insight and comments to improve this paper.

Deleted: (

Deleted:)

7. Appendix A: Balloon-Borne RO Cases and Sampling

Balloon-borne RO can collect high density observations around the platform, particularly compared to spaceborne RO. As was discussed in Section 2a, the Piksi GNSS receiver onboard World View balloon could observe a predicted total of 680 potential occultations. Because of frequency restrictions built into the Piksi receiver, signals from GLONASS, BeiDou, QZSS, and Galileo are less reliable due to slight frequency differences compared to the GPS system.

Figure A1 shows a Sankey plot filtering visualization of the World View predicted occultations. Of the original 680 predicted ROs, a total of 485 were incomplete from all

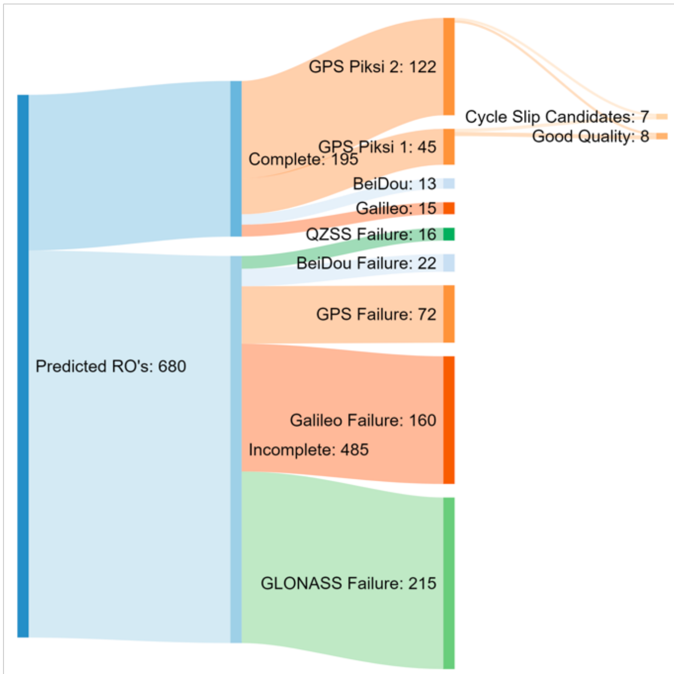

Figure A1: Sankey filtering plot visualizing the balloon-borne RO case filtering.

available GNSS satellite constellations. The remaining 195 occultations then filter further by removing those from QZSS, Galileo, BeiDou, and GLONASS with low quality due to the frequency tuning inherent to the Piksi receiver. Of the 167 from the GPS system, only 8 good quality cases were ready to use immediately. Another 7 cases required additional pre-processing in the form of cycle-slip corrections. The same process was also applied for cases observed during the ZPM-1 flight campaign.

Deleted: some

Deleted: During post-processing, 4 cases were removed for various quality control reasons, leaving the final 11 cases presented in Section 4.

8. References

Adhikari, L., Xie, F., and Haase, J. S.: Application of the full spectrum inversion algorithm to simulated airborne GPS radio occultation signals, Atmospheric Measurement Techniques, 9, 5077–5087, https://doi.org/10.5194/amt-9-5077-2016, 2016.

Anthes, R. A., Bernhardt, P. A., Chen, Y., Cucurull, L., Dymond, K. F., Ector, D., Healy, S. B., Ho, S. P., Hunt, D. C., Kuo, Y. H., Liu, H., Manning, K., McCormick, C., Meehan, T. K., Randel, W. J., Rocken, C., Schreiner, W. S., Sokolovskiy, S. V., Syndergaard, S., Thompson, D. C., Trenberth, K. E., Wee, T. K., Yen, N. L., and Zeng, Z.: The COSMIC/FORMOSAT-3 Mission: Early Results, Bulletin of the American Meteorological Society, 89, 313–334, https://doi.org/10.1175/bams-89-3-313, 2008.

Ao, C. O., Hajj, G. A., Meehan, T. K., Dong, D., Iijima, B. A., Mannucci, A. J., and Kursinski, E. R.: Rising and setting GPS occultations by use of open-loop tracking, Journal of Geophysical Research, 114, https://doi.org/10.1029/2008jd010483, 2009.

Boullot, N., Rabier, F., Langland, R., Gelaro, R., Cardinali, C., Guidard, V., Bauer, P., and Doerenbecher, A.: Observation impact over the southern polar area during the Concordiasi field campaign, Quarterly Journal of the Royal Meteorological Society, 142, 597–610, https://doi.org/10.1002/qj.2470, 2014.

Bowler, N. E.: An assessment of GNSS radio occultation data produced by Spire, Quarterly Journal of the Royal Meteorological Society, 146, 3772–3788, https://doi.org/10.1002/qj.3872, 2020.

Cardinali, C. and Healy, S.: Impact of GPS radio occultation measurements in the ECMWF system using adjoint-based diagnostics: Impact of GPS radio occultation measurements, Q.J.R. Meteorol. Soc., 140, 2315–2320, https://doi.org/10.1002/qj.2300, 2014.

Carreno-Luengo, H., Camps, A., Querol, J., and Forte, G.: First Results of a GNSS-R Experiment From a Stratospheric Balloon Over Boreal Forests, IEEE Transactions on Geoscience and Remote Sensing, 54, 2652–2663, https://doi.org/10.1109/tgrs.2015.2504242, 2016.

Chan, B. C., Goel, A., Kosh, J., Reid, T. G. R., Snyder, C. R., Tarantino, P. M., Soedarmadji, S., Soedarmadji, W., Nelson, K. J., Xie, F., and Vergalla, M.: GNSS Radio Occultation on Aerial Platforms with Commercial Off-the-Shelf Receivers, ION GNSS Proceedings, 2021.

Chan, B. C., Goel, A., Kosh, J., Reid, T. G. R., Snyder, C. R., Tarantino, P. M., Soedarmadji, S., Soedarmadji, W., Nelson, K. J., Xie, F., and Vergalla, M.: Commercial GNSS Radio Occultation on Aerial Platforms with Off-The-Shelf Receivers, Navigation, 2022.

Fjeldbo, G. and Eshleman, V. R.: Atmosphere of Venus as Studied with the Mariner 5 Dual Radio-Frequency Occultation Experiment, Radio Science, 4, 879–897, https://doi.org/10.1029/RS004i010p00879, 1969.

Fjeldbo, G., Kliore, A. J., and Eshleman, V. R.: The neutral atmosphere of Venus as studied with the Mariner V radio occultation experiments, The Astronomical Journal, 76, 123, 1971.

Garrison, J. L., Walker, M., Haase, J. S., Lulich, T., Xie, F., Ventre, B., Boehme, M. H., Wilmhoff, B., and Katzberg, S. J.: Development and Testing of the GISMOS Instrument, IEEE International, 2007.

Gelaro, R.: GEOS-5 Data Assimilation and Forecast Impacts for Concordiasi, THORPEX DAOS Working Group, 2011.

Haase, J. S., Maldonado-Vargas, J., Rabier, F., Cocquerez, P., Minois, M., Guidard, V., Wyss, P., and Johnson, A. V.: A proof-of-concept balloon-borne Global Positioning System radio occultation profiling instrument for polar studies, Geophysical Research Letters, 39, n/a-n/a, https://doi.org/10.1029/2011gl049982, 2012.

Harnisch, F., Healy, S. B., Bauer, P., and English, S. J.: Scaling of GNSS Radio Occultation Impact with Observation Number Using an Ensemble of Data Assimilations, Monthly Weather Review, 141, 4395–4413, https://doi.org/10.1175/mwr-d-13-00098.1, 2013.

Healy, S. B., Haase, J. S., and Lesne, O.: Abel transform inversion of radio occultation measurements made with a receiver inside the Earth's atmosphere, Annales Geophysicae, 20, 2002.

Hersbach, H., Bell, B., Berrisford, P., Hirahara, S., Horányi, A., Muñoz-Sabater, J., Nicolas, J., Peubey, C., Radu, R., Schepers, D., Simmons, A., Soci, C., Abdalla, S., Abellan, X., Balsamo, G., Bechtold, P., Biavati, G., Bidlot, J., Bonavita, M., De Chiara, G., Dahlgren, P., Dee, D., Diamantakis, M., Dragani, R., Flemming, J., Forbes, R., Fuentes, M., Geer, A., Haimberger, L., Healy, S., Hogan, R. J., Hólm, E., Janisková, M., Keeley, S., Laloyaux, P., Lopez, P., Lupu, C., Radnoti, G., de Rosnay, P., Rozum, I., Vamborg, F., Villaume, S., and Thépaut, J.-N.: The ERA5 Global Reanalysis, Quarterly Journal of the Royal Meteorological Society, 146, 1999–2049, https://doi.org/10.1002/qj.3803, 2020.

Ho, S., Anthes, R. A., Ao, C. O., Healy, S., Horanyi, A., Hunt, D., Mannucci, A. J., Pedatella, N., Randel, W. J., Simmons, A., Steiner, A., Xie, F., Yue, X., and Zeng, Z.: The COSMIC/FORMOSAT-3 Radio Occultation Mission after 12 Years: Accomplishments, Remaining Challenges, and Potential Impacts of COSMIC-2, Bulletin of the American Meteorological Society, 101, E1107–E1136, https://doi.org/10.1175/bams-d-18-0290.1, 2020.

Høeg, P., Hauchecorne, A., Kirchengast, G., Syndergaard, S., Belloul, B., Leitinger, R., and Rothleitner, W.: Derivation of Atmospheric Properties using a Radio Occultation Technique, Danish Meteorological Institute, Copenhagen, Denmark, 1996.

Imamura, T., Ando, H., Tellmann, S., Pätzold, M., Häusler, B., Yamazaki, A., Sato, T. M., Noguchi, K., Futaana, Y., Oschlisniok, J., Limaye, S., Choudhary, R. K., Murata, Y., Takeuchi, H., Hirose, C., Ichikawa, T., Toda, T., Tomiki, A., Abe, T., Yamamoto, Z., Noda, H., Iwata, T., Murakami, S., Satoh, T., Fukuhara, T., Ogohara, K., Sugiyama, K., Kashimura, H., Ohtsuki, S., Takagi, S., Yamamoto, Y., Hirata, N., Hashimoto, G. L., Yamada, M., Suzuki, M., Ishii, N., Hayashiyama, T., Lee, Y. J., and Nakamura, M.: Initial performance of the radio occultation experiment in the Venus orbiter mission Akatsuki, Earth, Planets and Space, 69, https://doi.org/10.1186/s40623-017-0722-3, 2017.

Jensen, A. S., Lohmann, M. S., Benzon, H.-H., and Nielsen, A. S.: Full Spectrum Inversion of radio occultation signals, Radio Science, 38, n/a-n/a, https://doi.org/10.1029/2002rs002763, 2003.

Kliore, A. J., Cain, D. L., Fjeldbo, G., Seidel, B. L., Sykes, M. J., and Rasool, S. I.: The Atmosphere of Mars from Mariner 9 Radio Occultation Measurements, Icarus, 17, 484–516, 1972.

Kursinski, E. R., Hajj, G. A., Bertiger, W. I., Leroy, S. S., Meehan, T. K., Romans, L. J., Schofield, J. T., McCleese, D. J., Melbourne, W. G., Thornton, C. L., Yunck, T. P., Eyre, J. R., and Nagafini, R. N.: Initial Results of Radio Occultation Observations of Earth's Atmosphere Using the Global Positioning System, Science, 271, 1107–1110, 1996.

Kursinski, E. R., Hajj, G. A., Schofield, J. T., Linfield, R. P., and Hardy, K. R.: Observing Earth's atmosphere with radio occultation measurements using the Global Positioning System, Journal of Geophysical Research: Atmospheres, 102, 23429–23465, https://doi.org/10.1029/97jd01569, 1997.

Kursinski, E. R., Hajj, G. A., Leroy, S. S., and Herman, B.: The GPS Radio Occultation Technique, Terrestrial, Atmospheric, and Oceanic Sciences, 11, 53–114, 2000.

Lesne, O., Haase, J. S., Kirchengast, G., Ramsauer, J., and Poetzi, W.: Sensitivity analysis for airborne sounding of the troposphere by GNSS radio occultation, Physics and Chemistry of the Earth, 27, 2002.

Lindal, G. F.: The atmosphere of Neptune-an analysis of radio occultation data acquired with Voyager 2, The Astronomical Journal, 103, 967–982, 1992.

Lindal, G. F., Hotz, H. B., Sweetnam, D. N., Shippony, Z., Brenkle, J. P., Hartsell, G. V., Spear, R. T., and Michael, W. H.: Viking radio occultation measurements of the atmosphere and topography of Mars: Data acquired during 1 Martian year of tracking, Journal of Geophysical Research, 84, https://doi.org/10.1029/JB084iB14p08443, 1979.

Luntama, J.-P., Kirchengast, G., Borsche, M., Foelsche, U., Steiner, A., Healy, S., von Engeln, A., O'Clerigh, E., and Marquardt, C.: Prospects of the EPS GRAS Mission for Operational Atmospheric Applications, Bulletin of the American Meteorological Society, 89, 1863–1875, https://doi.org/10.1175/2008BAMS2399.1, 2008.

Murphy, B. J., Haase, J. S., Muradyan, P., Garrison, J. L., and Wang, K. N.: Airborne GPS radio occultation refractivity profiles observed in tropical storm environments, Journal of Geophysical Research: Atmospheres, 120, 1690–1709, https://doi.org/10.1002/2014jd022931, 2015.

National Academies of Sciences, E.: Thriving on Our Changing Planet: A Decadal Strategy for Earth Observation from Space, The National Academies Press, Washington, DC, 2018.

National Oceanic and Atmospheric Administration and National Environmental Satellite, Data, and Information Service: Commercial Weather Data Pilot (CWDP) Round 2 Summary, 2020.

Rabier, F., Bouchard, A., Brun, E., Doerenbecher, A., Guedj, S., Guidard, V., Karbou, F., Peuch, V.-H., El Amraoui, L., Puech, D., Genthon, C., Picard, G., Town, M., Hertzog, A., Vial, F., Cocquerez, P., Cohn, S. A., Hock, T., Fox, J., Cole, H., Parsons, D., Powers, J., Romberg, K., VanAndel, J., Deshler, T., Mercer, J., Haase, J. S., Avallone, L., Kalnajs, L., Mechoso, C. R., Tangborn, A., Pellegrini, A., Frenot, Y., Thépaut, J.-N., McNally, A., Balsamo, G., and Steinle, P.: The Concordiasi Project in Antarctica, Bulletin of the American Meteorological Society, 91, 69–86, https://doi.org/10.1175/2009bams2764.1, 2010.

Rabier, F., Cohn, S., Cocquerez, P., Hertzog, A., Avallone, L., Deshler, T., Haase, J., Hock, T., Doerenbecher, A., Wang, J., Guidard, V., Thépaut, J.-N., Langland, R., Tangborn, A., Balsamo, G., Brun, E., Parsons, D., Bordereau, J., Cardinali, C., Danis, F., Escarnot, J.-P., Fourrié, N., Gelaro, R., Genthon, C., Ide, K., Kalnajs, L., Martin, C., Meunier, L.-F., Nicot, J.-M., Perttula, T., Potts, N., Ragazzo, P., Richardson, D., Sosa-Sesma, S., and Vargas, A.: The Concordiasi Field Experiment over Antarctica: First Results from Innovative Atmospheric Measurements, Bulletin of the American Meteorological Society, 94, ES17–ES20, https://doi.org/10.1175/bams-d-12-00005.1, 2013.

Ruston, B. and Healy, S.: Forecast Impact of FORMOSAT-7/COSMIC-2 GNSS Radio Occultation Measurements, Atmospheric Science Letters, 22, https://doi.org/10.1002/asl.1019, 2020.

Schreiner, W. S., Weiss, J. P., Anthes, R. A., Braun, J., Chu, V., Fong, J., Hunt, D., Kuo, Y.-H., Meehan, T., Serafino, W., Sjoberg, J., Sokolovskiy, S., Talaat, E., Wee, T. K., and Zeng, Z.: COSMIC-2 Radio Occultation Constellation: First Results, Geophysical Research Letters, 47, https://doi.org/10.1029/2019gl086841, 2020.

Shi, J. Q. and Choi, T.: Gaussian Process Regression Analysis for Functional Data, CRC Press, Boca Raton, FL, USA, 2011.

Vorob'ev, V. V. and Krasil'nikova, T. G.: Estimation of the Accuracy of the Atmospheric Refractive Index Recovery from Doppler Shift Measurements at Frequencies Used in the NAVSTAR System, Physics of the Atmosphere and Ocean, 29, 1994.

Wang, K.-N., Muradyan, P., Garrison, J. L., Haase, J. S., Murphy, B., Acikoz, U., and Lulich, T.: Open-loop tracking of rising and setting GNSS radio-occultation signals from an Airborne Platform: Signal model and statistical analysis, IGARSS Proceedings, 3367–3370, https://doi.org/10.1109/IGARSS.2013.6723550, 2013.

Wang, K.-N., Garrison, J. L., Acikoz, U., Haase, J. S., Murphy, B. J., Muradyan, P., and Lulich, T.: Open-Loop Tracking of Rising and Setting GPS Radio-Occultation Signals From an Airborne Platform: Signal Model and Error Analysis, IEEE Transactions on Geoscience and Remote Sensing, 54, 3967–3984, https://doi.org/10.1109/tgrs.2016.2532346, 2016.

Ware, R. H., Exner, M., Feng, D., Gorbunov, M., Hardy, K. R., Herman, B., Kuo, Y. H., Meehan, T. K., Melbourne, W., Rocken, C., Schreiner, W. S., Sokolovskiy, S., Solheim, F., Zou, X., Anthes, R., Businger, S., and Trenberth, K. E.: GPS Sounding of the Atmosphere from Low Earth Orbit: Preliminary Results, Bulletin of the American Meteorological Society, 77, 19–40, 1996.

Xie, F., Haase, J. S., and Syndergaard, S.: Profiling the Atmosphere Using the Airborne GPS Radio Occultation Technique: A Sensitivity Study, IEEE Transactions on Geoscience and Remote Sensing, 46, 3424–3435, https://doi.org/10.1109/tgrs.2008.2004713, 2008.

Xie, F., Adhikari, L., Haase, J. S., Murphy, B., Wang, K.-N., and Garrison, J. L.: Sensitivity of airborne radio occultation to tropospheric properties over ocean and land, Atmospheric Measurement Techniques, 11, 763–780, https://doi.org/10.5194/amt-11-763-2018, 2018.

Zuffada, C., Hajj, G. A., and Kursinski, E. R.: A novel approach to atmospheric profiling with a mountain-based or airborne GPS receiver, Journal of Geophysical Research: Atmospheres, 104, 24435–24447, https://doi.org/10.1029/1999jd900766, 1999.